

# Topological Superconductivity in $\text{Cu}_x\text{Bi}_2\text{Se}_3$

Satoshi Sasaki,<sup>1</sup> M. Kriener,<sup>1</sup> Kouji Segawa,<sup>1</sup> Keiji Yada,<sup>2</sup> Yukio Tanaka,<sup>2</sup> Masatoshi Sato,<sup>3</sup> and Yoichi Ando<sup>1,\*</sup>

<sup>1</sup>*Institute of Scientific and Industrial Research, Osaka University, Ibaraki, Osaka 567-0047, Japan*

<sup>2</sup>*Department of Applied Physics, Nagoya University, Nagoya 464-8603, Japan*

<sup>3</sup>*Institute for Solid State Physics, University of Tokyo, Chiba 277-8581, Japan*

(Dated: October 23, 2018)

A topological superconductor (TSC) is characterized by the topologically-protected gapless surface state that is essentially an Andreev bound state consisting of Majorana fermions. While a TSC has not yet been discovered, the doped topological insulator  $\text{Cu}_x\text{Bi}_2\text{Se}_3$ , which superconducts below  $\sim 3$  K, has been predicted to possess a topological superconducting state. We report that the point-contact spectra on the cleaved surface of superconducting  $\text{Cu}_x\text{Bi}_2\text{Se}_3$  present a zero-bias conductance peak (ZBCP) which signifies unconventional superconductivity. Theoretical considerations of all possible superconducting states help us conclude that this ZBCP is due to Majorana Fermions and gives evidence for a topological superconductivity in  $\text{Cu}_x\text{Bi}_2\text{Se}_3$ . In addition, we found an unusual pseudogap that develops below  $\sim 20$  K and coexists with the topological superconducting state.

PACS numbers: 74.45.+c, 74.20.Rp, 73.20.At, 03.65.Vf

The recent discovery of the topological insulator [1–24] stimulated the search for an even more exotic state of matter, the topological superconductor (TSC) [25–28]. A topological state of matter is characterized by a topological structure of the quantum-mechanical wavefunction in the Hilbert space. In topological insulators, a non-trivial  $Z_2$  topology of the bulk valence band leads to the emergence of Dirac fermions on the surface [22, 23]. Similarly, in TSCs non-trivial  $Z$  or  $Z_2$  topologies of the superconducting (SC) states lead to the appearance of Majorana fermions on the surface [25–27]. Majorana fermions are peculiar in that particles are their own antiparticles, and they were originally conceived as mysterious neutrinos [29]. Currently their realization in condensed matter is of significant interest because of their novelty as well as the potential for quantum computing [29].

The  $\text{Cu}_x\text{Bi}_2\text{Se}_3$  superconductor [30–33] is a prime candidate of TSC because of its peculiar band structure and strong spin-orbit coupling [34]. In this material, Cu atoms are intercalated into the layered topological insulator  $\text{Bi}_2\text{Se}_3$  and the SC state appears for the Cu concentration  $x$  of about 0.2 – 0.5, which causes electron doping with the density of  $\sim 10^{20} \text{ cm}^{-3}$ . This material has not been well studied because of the difficulty in preparing high-quality samples [30, 31] but a recent breakthrough in the synthesis of  $\text{Cu}_x\text{Bi}_2\text{Se}_3$  by using electrochemistry [32, 33] made it possible to prepare reliable junctions and perform a conductance spectroscopy in the superconducting state.

In the present work, we employed the so-called “soft” point-contact technique [35]: The contacts were prepared at room temperature in ambient atmosphere by putting a tiny ( $\sim 20 \mu\text{m}$ ) drop of silver paste on the cleaved (111) surface of a  $\text{Cu}_x\text{Bi}_2\text{Se}_3$  single crystal below a  $30\text{-}\mu\text{m}$ -diameter gold wire [Figs. 1(a) and 1(b)]. In this type of junctions, ballistic transport occurs sporadically through parallel nanometer-scale channels formed between indi-

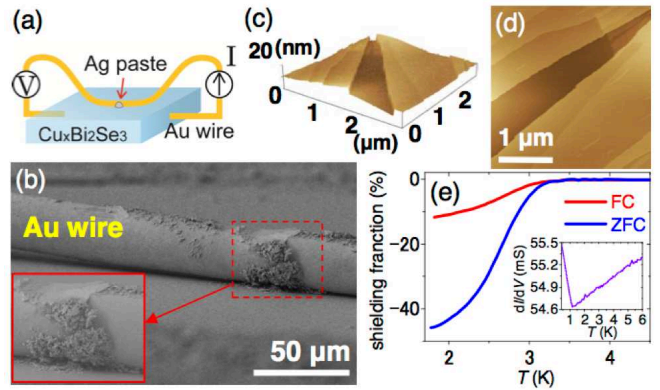


FIG. 1: (Color online) Point-contact experiment and the sample. (a) Sketch of the “soft” point contact and the measurement circuit. (b) Scanning-electron-microscope picture of the actual sample; inset magnifies the silver-paste spot where the point contact is formed. (c) 3D presentation of nanometer-scale terraces on a typical cleaved surface of  $\text{Cu}_x\text{Bi}_2\text{Se}_3$  seen by an atomic-force microscope. Typical terrace width is  $0.5 \mu\text{m}$ . (d) A false color mapping of (c). (e) SQUID data for the SC transition in the sample ( $x = 0.3$ ) used for the point-contact measurements shown in Fig. 2. Both the zero-field-cooled (ZFC) and the field-cooled (FC) data measured in  $0.2 \text{ mT}$  are shown, and the former gives the SC shielding fraction of  $46\%$ . Inset shows the temperature dependence of the zero-bias differential conductance of the point contact reported in Fig. 2.

vidual grains in the silver paste and the sample surface [see Figs. 1(c), 1(d) and Ref. 36]. The  $dI/dV$  spectra were measured with a lock-in technique by sweeping a dc current that is superimposed with a small-amplitude ac current [ $1.35 \mu\text{A}$  (rms), corresponding to  $0.5 \text{ A/cm}^2$ ]. We used a quasi-four-probe configuration, in which the current was applied between a contact pad and the gold wire, and the voltage between the wire and another contact pad was measured [Fig. 1(a)]. The Quantum Design

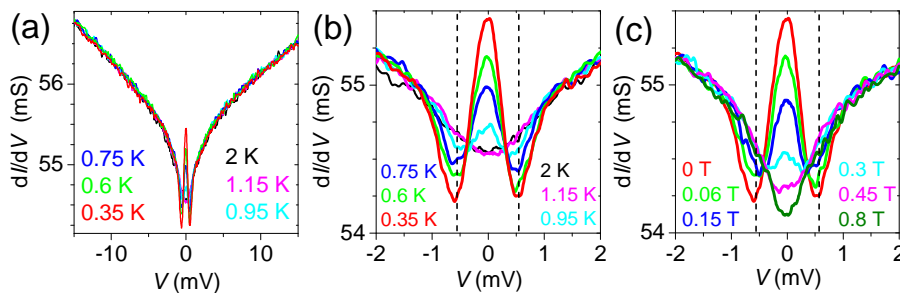


FIG. 2: (Color online) Zero-bias conductance peak. (a) Point-contact spectra ( $dI/dV$  vs bias voltage) of  $\text{Cu}_x\text{Bi}_2\text{Se}_3$  with  $x = 0.3$  for 0.35–2 K measured in 0 T for a wide energy window. (b) A narrower window of (a). (c) The spectra at 0.35 K measured in perpendicular magnetic fields of 0–0.8 T. The vertical dashed lines in (b) and (c) indicate the energy position of the dips.

PPMS was used for cooling the samples down to 0.35 K and applying the magnetic field up to 9 T.

A set of point-contact data taken on a  $\text{Cu}_x\text{Bi}_2\text{Se}_3$  sample with the bulk onset  $T_c = 3.2$  K is shown in Fig. 2, where one can see that a pronounced zero-bias conductance peak (ZBCP) develops at low temperature [36]. The inset of Fig. 1(e) shows the temperature dependence of the zero-bias conductance, which indicates that this peak appears below 1.2 K [36]. We note that essentially the same ZBCP data have been obtained on another sample (see Fig. S2 of Ref. 36).

Since heating effects can cause a spurious ZBCP [37], it is important to elucidate that it is not the case here. It was argued by Sheet *et al.* [37] that in samples with a large normal-state resistivity when the point contact is in the thermal regime, a spurious ZBCP could show up if the increase in the bias voltage causes the local current to exceed the critical current, which leads to a voltage-dependent decrease in the differential conductivity. If this is the case, the conductivity at zero bias (which is always measured below the critical current) should *not* change with a weak magnetic field; the role of the magnetic field in this case is primarily to reduce the critical current, so the width of the spurious ZBCP would become narrower, but the height at  $V = 0$  should be mostly unchanged as long as the superconductor is in the zero-resistivity state. In the magnetic-field dependence of our spectra shown in Fig. 2(c), by contrast, the ZBCP is strongly suppressed with a modest magnetic field while its width is little affected, which clearly speaks against the heating origin of the ZBCP. (The magnetic field was applied perpendicular to the cleaved surface.) Another well-known signature of the heating effect is a sharp, spike-like dip at energies much larger than the gap [35, 37], which is caused by the local transition to normal state; in fact, when we made the point contact on a disordered surface, we observed a widening of the peak and a lot of sharp dips at relatively high energies, which are obviously caused by the heating [36]. In contrast, the data shown in Fig. 2 are free from such features, which

corroborates the intrinsic nature of the ZBCP. Therefore, one can safely conclude that the ZBCP observed here is not due to the heating effects and is intrinsic.

One should also keep in mind that, even when the ZBCP is intrinsic, it can be caused by several mechanisms in point contacts [38]: conventional Andreev reflection [39, 40], reflectionless tunneling [41–43], magnetic scattering [44, 45], and the unconventional Andreev bound state (ABS) [38, 40]. In this respect, it is important to notice that the ZBCP shown in Fig. 2 is accompanied by pronounced dips on its sides and the peak does not split into two even at the lowest temperature (0.35 K). These features are clearly at odds with the Blonder-Tinkham-Klapwijk (BTK) theory for conventional Andreev reflection [39]. Also, the reflectionless tunneling and the magnetic scattering are obviously irrelevant, because the former is suppressed by a very small magnetic field of less than 0.1 T [46] and the latter presents a peak splitting in magnetic fields [47]. Hence, one can conclude that the ZBCP observed here is a manifestation of the ABS [38].

Previously, it was inferred [32] from the specific-heat data that the superconducting gap of  $\text{Cu}_x\text{Bi}_2\text{Se}_3$  at  $T = 0$  K,  $\Delta(0)$ , would be about 0.7 meV. In Fig. 2, one can see that the minima in the pronounced dips are located at  $\sim \pm 0.6$  meV at 0.35 K; since the ZBCP due to the ABS is usually accompanied by dips near the gap energy [38], the energy scale of the dip is assuring.

Given that the observed ZBCP is intrinsic and is due to the ABS, it is important to understand its concrete origin. The ABS is caused by the interference of the SC wavefunction at the surface, and it is a signature of unconventional superconductivity [38]. Its occurrence is determined by the symmetry of the SC state, which in turn is determined by the symmetry of the Hamiltonian and the pairing mechanism. Also, it has been elucidated that Majorana fermions reside in an ABS when it is spin non-degenerate [48]. Hence, we examined all possible SC states in  $\text{Cu}_x\text{Bi}_2\text{Se}_3$  and the nature of the ABS to elucidate whether the observed ZBCP is due to Majorana

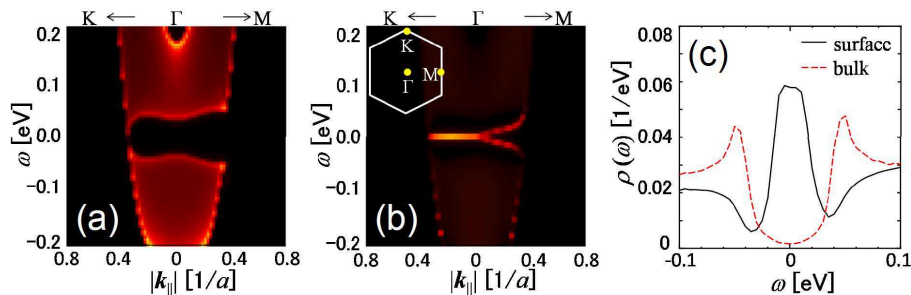


FIG. 3: (Color online) Model calculations of the topological band structure in the superconducting state of  $\text{Cu}_x\text{Bi}_2\text{Se}_3$ . Theoretically calculated spectral functions  $A(\mathbf{k}, \omega)$  of the bulk (a) and the surface on the  $xy$  plane (b) in  $\Gamma$ -M and  $\Gamma$ -K directions in the surface Brillouin zone shown in the inset of (b), as well as the LDOS (c), in the superconducting state for the topological gap function  $\Delta_4$  ( $\Delta_{\uparrow\uparrow}^{12} = \Delta_{\downarrow\downarrow}^{12} = -\Delta_{\uparrow\uparrow}^{21} = -\Delta_{\downarrow\downarrow}^{21}$ ); the model Hamiltonian and the band parameters used are described in detail in Ref. 36. The false colour mappings of  $A(\mathbf{k}, \omega)$  in (a) and (b) are in arbitrary units.  $\Delta(0)$  was set to be 0.05 eV for the convenience of the calculations.

rana fermions. The microscopic model to describe the band structure of  $\text{Cu}_x\text{Bi}_2\text{Se}_3$  has already been developed [34, 49–51], and it was shown [34] that, if both short- and long-range interactions are considered, the symmetry of the Hamiltonian allows four different types of the SC gap function,  $\Delta_1$  to  $\Delta_4$  [36], with three of them being unconventional. Following Ref. 51, we have theoretically calculated the spectral functions of the bulk and the surface as well as the local functions of the states (LDOS) for all possible gap functions (see Ref. 36 for details), similar to those done in Refs. 52 and 53.

Firstly, the conventional even-parity SC state  $\Delta_1$  was found to give no two-dimensional (2D) ABS [36]. While in this case the surface could become a 2D TSC due to the proximity effect as proposed by Fu and Kane [28], the surface of a three-dimensional (3D) superconductor is continuously connected and has no topological edge; hence, the one-dimensional Majorana fermions that might appear at the edge of a 2D TSC [28] would not exist in the present case.

Among the remaining three possible SC states that are all unconventional, the fully-gapped, odd-parity SC state  $\Delta_2$  gives rise to 2D helical Majorana fermions as the ABS. However, because of the Dirac-like dispersion of this ABS, the surface LDOS tends to have a minimum at zero energy [36], which does not agree well with our data; nevertheless, it was very recently proposed that the ZBCP could appear even in this fully-gapped state due to a peculiar “twisting” of the ABS dispersion [54]. In the case of the other two odd-parity SC states,  $\Delta_3$  and  $\Delta_4$ , both of which have two point nodes, a single ZBCP naturally shows up in the surface LDOS [Figs. 3(a) – 3(c)]; this is because the point nodes lead to a partially flat dispersion of the helical Majorana fermions, concentrating the LDOS near zero energy. Therefore, it is most likely that the observed ZBCP signifies 2D Majorana fermions due to the odd-parity bulk SC state, although it is difficult to determine the exact pairing state from the three possibilities at this stage. The fact that

the ZBCP is strongly suppressed with a modest magnetic field [Fig. 2(c)] supports this conclusion, because the helical Majorana fermions are naturally suppressed as the time-reversal symmetry is broken with the magnetic field. Note that, while there are nanometer-scale terraces on the cleaved surface [Figs. 1(c), 1(d) and Ref. 36], electron transmissions in the in-plane directions through the side walls of the terraces are much less likely to take place compared to the transmissions in the out-of-plane direction, because the typical terrace height ( $< 10$  nm) is much smaller than the typical Ag grain size of 50 nm [36]. Therefore, our data are expected to reflect mostly the ABS on the (111) surface.

We now discuss the topological nature of the possible SC states  $\Delta_3$  and  $\Delta_4$ . The presence of the point nodes might seem to preclude the topological superconductivity, which is usually considered to require a full gap. However, for the  $\Delta_3$  and  $\Delta_4$  states one can define a non-trivial topological invariant, “mod-2 winding number”, which is immune to weak perturbations and assures that the  $\Delta_3$  and  $\Delta_4$  states are robustly topological [36]. In fact, a time-reversal-invariant SC state with a pair of point nodes is adiabatically connected to a fully-gapped state in the “mod-2 winding number” topological class, and having an odd parity is sufficient for this case to become topologically non-trivial [36].

Previously, we reported that the specific-heat data was most consistent with a fully-gapped SC state [32]. It is fair to note, however, that the entropy contribution of the quasiparticles excited near the point node of a 3D SC state is very small and, indeed, the  $T^3$  dependence of the specific heat expected for point nodes is difficult to be distinguished [55], particularly in inhomogeneous samples. Therefore, the  $\Delta_3$  or  $\Delta_4$  state with point nodes does not necessarily contradict the existing specific-heat data.

An interesting and unexpected feature in our data is that a pseudogap develops below  $\sim 20$  K [Fig. 4(a)]. As shown in Figs. 4(b) – 4(g), this pseudogap appears to

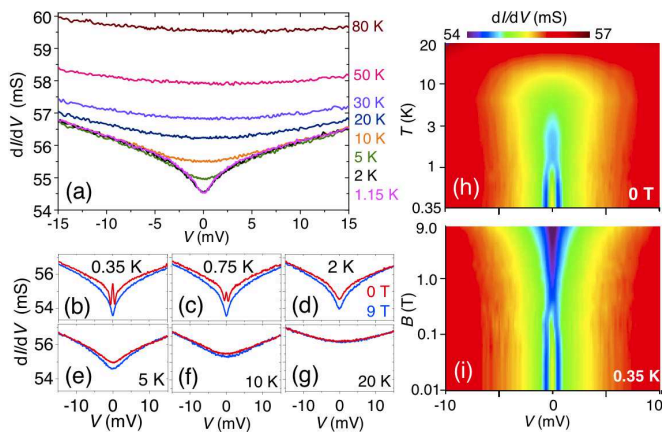


FIG. 4: (Color online) Pseudogap in  $\text{Cu}_x\text{Bi}_2\text{Se}_3$ . (a)  $dI/dV$  vs bias voltage for 1.15–80 K measured in 0 T. (b – g) Comparisons of the spectra in 0 and 9 T. At low temperature below  $\sim 20$  K, the spectra in 9 T show smaller  $dI/dV$  near zero bias compared to that at 0 T, indicating that the pseudogap deepens with the magnetic field. (h, i) False colour mappings of  $dI/dV$  in the bias-voltage vs temperature plane in 0 T (h) and in the bias-voltage vs magnetic-field plane at 0.35 K (i), summarizing how the spectra change with temperature and magnetic field; note that the vertical axes are in logarithmic scales in both (h) and (i).

be enhanced by the magnetic field, and it is most pronounced at 0.35 K in high magnetic fields. This pseudogap coexists with the superconductivity below the upper critical field  $H_{c2}$  [56] and may give us a clue to understanding the pairing mechanism in  $\text{Cu}_x\text{Bi}_2\text{Se}_3$ . Finally, how the spectra change with temperature and magnetic field is summarized in false colour mappings shown in Figs. 4(h) and 4(i).

As is clear from the above discussions, one can conclude that the ZBCP in  $\text{Cu}_x\text{Bi}_2\text{Se}_3$  signifies an ABS consisting of 2D Majorana fermions and that  $\text{Cu}_x\text{Bi}_2\text{Se}_3$  is hosting a topological superconductivity. It is therefore an urgent task to determine the exact pairing symmetry in  $\text{Cu}_x\text{Bi}_2\text{Se}_3$ . Regarding the Majorana physics, an interesting question is the existence of the Majorana zero-mode in the vortex core [57]. The 2D Majorana fermions living on the surface of a 3D TSC are different from the non-Abelian Majorana fermions of a 2D TSC proposed for topological quantum computing [22, 28], but establishing a general understanding of Majorana fermions is important for both fundamental physics and future information technologies.

In summary, our point-contact spectroscopy of the  $\text{Cu}_x\text{Bi}_2\text{Se}_3$  superconductor found an unusual pseudogap below  $\sim 20$  K and a pronounced ZBCP in the SC state. The latter signifies an unconventional SC state that can only be topological in  $\text{Cu}_x\text{Bi}_2\text{Se}_3$ , and therefore our observation gives evidence for a topological superconductivity in this material. One can fully expect that  $\text{Cu}_x\text{Bi}_2\text{Se}_3$  as the first concrete example of a TSC will greatly help

advance our understanding of topological states of matter and associated exotic quasiparticles.

We thank L. Fu, A. Furusaki and S. Onoda for useful discussions, and K. Matsumoto and S. Wada for their help in the experiment. This work was supported by JSPS (NEXT Program), MEXT (Innovative Area “Topological Quantum Phenomena” KAKENHI), and AFOSR (AOARD 10-4103).

\* Electronic address: y'ando@sanken.osaka-u.ac.jp

- [1] C. L. Kane and E. J. Mele, Phys. Rev. Lett. **95**, 146802 (2005).
- [2] B. A. Bernevig, T. L. Hughes, and S.-C. Zhang, Science **314**, 1757 (2006).
- [3] M. König, S. Wiedmann, C. Brüne, A. Roth, H. Buhmann, L. W. Molenkamp, X.-L. Qi, S.-C. Zhang, Science **318**, 766 (2007).
- [4] L. Fu, C. L. Kane, and E. J. Mele, Phys. Rev. Lett. **98**, 106803 (2007).
- [5] J. E. Moore and L. Balents, Phys. Rev. B **75**, 121306(R) (2007).
- [6] R. Roy, Phys. Rev. B **79**, 195322 (2009).
- [7] X.-L. Qi, T. L. Hughes, and S.-C. Zhang, Phys. Rev. B **78**, 195424 (2008).
- [8] L. Fu and C. L. Kane, Phys. Rev. B **76**, 045302 (2007).
- [9] D. Hsieh, D. Qian, L. Wray, Y. Xia, Y. S. Hor, R. J. Cava, and M. Z. Hasan, Nature **452**, 970 (2008).
- [10] A. A. Taskin and Y. Ando, Phys. Rev. B **80**, 085303 (2009).
- [11] A. Nishide, A. A. Taskin, Y. Takeichi, T. Okuda, A. Kakizaki, T. Hirahara, K. Nakatsuji, F. Komori, Y. Ando, and I. Matsuda, Phys. Rev. B. **81**, 041309(R) (2010).
- [12] Y. L. Chen, J. G. Analytis, J.-H. Chu, Z. K. Liu, S.-K. Mo, X. L. Qi, H. J. Zhang, D. H. Lu, X. Dai, Z. Fang, S. C. Zhang, I. R. Fisher, Z. Hussain, and Z.-X. Shen, Science **325**, 178 (2009).
- [13] D. Hsieh, Y. Xia, D. Qian, L. Wray, F. Meier, J. H. Dil, J. Osterwalder, L. Patthey, A. V. Fedorov, H. Lin, A. Bansil, D. Grauer, Y. S. Hor, R. J. Cava, and M. Z. Hasan, Phys. Rev. Lett. **103**, 146401 (2009).
- [14] Y. Xia, D. Qian, D. Hsieh, L. Wray, A. Pal, H. Lin, A. Bansil, D. Grauer, Y. S. Hor, R. J. Cava, and M. Z. Hasan, Nat. Phys. **5**, 398 (2009).
- [15] T. Sato, K. Segawa, H. Guo, K. Sugawara, S. Souma, T. Takahashi, and Y. Ando, Phys. Rev. Lett. **105**, 136802 (2010).
- [16] K. Kuroda, M. Ye, A. Kimura, S. V. Ereemeev, E. E. Krasovskii, E. V. Chulkov, Y. Ueda, K. Miyamoto, T. Okuda, K. Shimada, H. Namatame, and M. Taniguchi, Phys. Rev. Lett. **105**, 146801 (2010).
- [17] Y. L. Chen, Z. K. Liu, J. G. Analytis, J.-H. Chu, H. J. Zhang, B. H. Yan, S.-K. Mo, R. G. Moore, D. H. Lu, I. R. Fisher, S.-C. Zhang, Z. Hussain, and Z.-X. Shen, Phys. Rev. Lett. **105**, 266401 (2010).
- [18] Z. Ren, A.A. Taskin, S. Sasaki, K. Segawa, and Y. Ando, Phys. Rev. B **82**, 241306(R) (2010).
- [19] S.Y. Xu, L.A. Wray, Y. Xia, R. Shankar, A. Petersen, A. Fedorov, H. Lin, A. Bansil, Y.S. Hor, D. Grauer, R.J. Cava, and M.Z. Hasan, arXiv:1007.5111v1.

- [20] J. Xiong, A.C. Petersen, Dongxia Qu, R. J. Cava, and N. P. Ong, arXiv:1101.1315.
- [21] A.A. Taskin, Z. Ren, S. Sasaki, K. Segawa, and Y. Ando, Phys. Rev. Lett. **107**, 016801 (2011).
- [22] M. Z. Hasan and C. L. Kane, Rev. Mod. Phys. **82**, 3045 (2010).
- [23] J. E. Moore, Nature (London) **464**, 194 (2010).
- [24] X.-L. Wang, S. X. Dou, and C. Zhang, NPG Asia Mater. **2**, 31 (2010).
- [25] X.-L. Qi and S.-C. Zhang, arXiv:1008.2026v1.
- [26] A. P. Schnyder, S. Ryu, A. Furusaki, and A. W. W. Ludwig, Phys. Rev. B **78**, 195125 (2008).
- [27] M. Sato, Phys. Rev. B **81**, 220504(R) (2010).
- [28] L. Fu and C. L. Kane, Phys. Rev. Lett. **100**, 096407 (2008).
- [29] F. Wilczek, Nature Phys. **5**, 614 (2009).
- [30] Y. S. Hor, A. J. Williams, J. G. Checkelsky, P. Roushan, J. Seo, Q. Xu, H. W. Zandbergen, A. Yazdani, N. P. Ong, and R.J. Cava, Phys. Rev. Lett. **104**, 057001 (2010).
- [31] L. A. Wray, S.-Y. Xu, Y. Xia, Y. S. Hor, D. Qian, A. V. Fedorov, H. Lin, A. Bansil, R. J. Cava, and M. Z. Hasan, Nature Phys. **6**, 855 (2010).
- [32] M. Kriener, K. Segawa, Z. Ren, S. Sasaki, and Y. Ando, Phys. Rev. Lett. **106**, 127004 (2011).
- [33] M. Kriener, K. Segawa, Z. Ren, S. Sasaki, S. Wada, S. Kuwabata, and Y. Ando, Phys. Rev. B **84**, 054513 (2011).
- [34] L. Fu and E. Berg, Phys. Rev. Lett. **105**, 097001 (2010).
- [35] D. Daghero and R. S. Gonnelli, Supercond. Sci. Technol. **23**, 043001 (2010).
- [36] See Supplemental Material at [URL will be inserted by publisher] for supplemental data and discussions.
- [37] G. Sheet, S. Mukhopadhyay, and P. Raychaudhuri, Phys. Rev. B **69**, 134507 (2004).
- [38] S. Kashiwaya and Y. Tanaka, Rep. Prog. Phys. **63**, 1641 (2000).
- [39] G. E. Blonder, M. Tinkham, and T. M. Klapwijk, Phys. Rev. B **25**, 4515 (1982).
- [40] G. Deutscher, Rev. Mod. Phys. **77**, 109 (2005).
- [41] A. Kastalsky, A. W. Kleinsasser, L. H. Greene, R. Bhat, F. P. Milliken, and J. P. Harbison, Phys. Rev. Lett. **67**, 3026 (1991).
- [42] C. W. J. Beenakker, Phys. Rev. B **46**, 12841 (1992); I. K. Marmorkos, C. W. J. Beenakker, and R. A. Jalabert, Phys. Rev. B **48**, 2811 (1993).
- [43] B. J. van Wees, P. de Vries, P. Magnée, and T. M. Klapwijk, Phys. Rev. Lett. **69**, 510 (1992).
- [44] J. A. Appelbaum, Phys. Rev. **154**, 633 (1967).
- [45] L. Y. L. Shen and J. M. Rowell, Phys. Rev. **165**, 566 (1968).
- [46] The footprint of our point contact is  $\sim 20 \mu\text{m}$ , which is larger than the dephasing length  $L_\phi$  of  $\sim 1 \mu\text{m}$  in Ag below 1 K [P. McConville and N. O. Birge, Phys. Rev. B **47**, 16667 (1993)]. This means that  $L_\phi$  governs the reflectionless tunneling [42] which would be suppressed with  $\sim 0.7$  mT.
- [47] The  $g$  factor of  $\text{Bi}_2\text{Se}_3$  is as large as 32 for  $H \parallel C_3$  [H. Köhler and E. Wöchner, Phys. Status Solidi B **67**, 665 (1975)], which suggests that the Zeeman splitting for  $S = 1/2$  in 0.1 T would be  $\sim 0.2$  meV. This should be observable if the magnetic scattering is relevant.
- [48] J. Linder, Y. Tanaka, T. Yokoyama, A. Sudbø, and N. Nagaosa, Phys. Rev. Lett. **104**, 067001 (2010).
- [49] H. Zhang, C.-X. Liu, X.-L. Qi, X. Dai, Z. Fang, and S. C. Zhang, Nature Phys. **5**, 438 (2009).
- [50] C.-X. Liu, X.-L. Qi, H. Zhang, X. Dai, Z. Fang, and S.-C. Zhang, Phys. Rev. B **82**, 045122 (2010).
- [51] L. Hao and T. K. Lee, Phys. Rev. B **83**, 134516 (2011).
- [52] A. P. Schnyder, P. M. R. Brydon, D. Manske, and C. Timm, Phys. Rev. B **82**, 184508 (2010).
- [53] K. Yada, M. Sato, Y. Tanaka, and T. Yokoyama, Phys. Rev. B **83**, 064505 (2011).
- [54] T. Hsieh and L. Fu, arXiv:1109.3464.
- [55] H. R. Ott, H. Rudigier, T. M. Rice, K. Ueda, Z. Fisk, and J. L. Smith, Phys. Rev. Lett. **52**, 1915 (1984).
- [56] With resistivity measurements, we confirmed that the SC state is completely suppressed with the perpendicular magnetic field of 3 T (with the midpoint  $H_{c2}$  of 1.7 T) at 0.35 K, consistent with the reported  $H_{c2}(T)$  diagram [32].
- [57] P. Hosur, P. Ghaemi, R. S. K. Mong, and A. Vishwanath, Phys. Rev. Lett. **107**, 097001 (2011).
- [58] V. J. Emery and S. A. Kivelson, Nature (London) **374**, 434 (1995).
- [59] Y. Tanaka, T. Yokoyama, and N. Nagaosa, Phys. Rev. Lett. **103**, 107002 (2009).
- [60] Y. Asano, Y. Tanaka, Y. Matsuda, and S. Kashiwaya, Phys. Rev. B **68**, 184506 (2003).
- [61] M. Sato and S. Fujimoto, Phys. Rev. Lett. **105**, 217001 (2010).
- [62] Z. Wang, X.-L. Qi, and S. C. Zhang, New J. Phys. **12**, 065007 (2010).
- [63] M. Sato, Phys. Rev. B **79**, 214526 (2009).

# Supplemental Material

## S1. Surface of $\text{Cu}_x\text{Bi}_2\text{Se}_3$ single-crystal samples

Although the cleaved surface of  $\text{Cu}_x\text{Bi}_2\text{Se}_3$  single crystals is essentially flat [Fig. S1(a)], there are a lot of nanometer-scale terraces as revealed by an atomic-force microscope [Figs. S1(b) and S1(c), and also Figs. 1(c) and 1(d) of the main text]. The heights of those terraces are often larger than the one quintuple-layer unit (0.95 nm) but are typically less than 10 nm. There is no clear preferential direction for the edges of the terraces. While there are several tens of terraces in the lateral area of a 20- $\mu\text{m}$  point contact in which nanometer-scale silver grains (typically 50-nm diameter) are distributed, electron transmissions into the Ag grains from the (111) surface is expected to be dominant because the typical terrace height ( $< 10$  nm) is much smaller than the typical Ag grain size (50 nm).

## S2. Reproducibility of the ZBCP

To demonstrate the reproducibility of the observed ZBCP, Figs. S2(a) and S2(b) present a set of point-contact spectra showing the ZBCP below 1 K, taken on another  $\text{Cu}_x\text{Bi}_2\text{Se}_3$  sample with the bulk onset  $T_c = 3.2$  K. At 0.35 K, the minima in the dips are located at about  $\pm 0.4$  meV, which suggests that the SC gap in this sample was a bit smaller compared to the sample shown in the main text.

We note that the chances of observing the ZBCP were not very high: We have so far measured 47 samples, and 25 of them showed no ZBCP down to 0.35 K (an example is shown in Fig. S3). In other words, 22 out of 47 samples have been found to present a ZBCP in our experiment. This seems to be correlated with the fact that our samples are inhomogeneous and show the SC shielding fractions of around 40%.

## S3. Onset temperature of the ZBCP

As mentioned in the main text, the enhancement of the zero-bias conductance of the sample reported in Fig. 2 occurred below 1.2 K, which is lower than the bulk onset  $T_c$  of 3.2 K. One possibility for this difference is that the ZBCP is prone to thermal smearing and needs a low temperature to become observable. Another possibility is that the  $T_c$  was locally 1.2 K at the position beneath the point contact; this is conceivable because the temperature dependence of the diamagnetic signal [Fig. 1(e)] suggests a broad distribution of local  $T_c$ . If this second possibility is actually the case, our observation that the energy scale of the dip in the point-contact spectra [0.6 meV, see Fig. 2(b)] agrees with the estimated bulk SC gap may suggest an interesting situation where the pair potential  $\Delta(0)$  is essentially the same in all the superconducting portions of the sample but the local  $T_c$  is determined by the local carrier density, because the carrier density in  $\text{Cu}_x\text{Bi}_2\text{Se}_3$  is very low and the  $T_c$  may well be governed by the superfluid density [58].

## S4. Effects of heating and/or critical currents on the point-contact spectra

When the point contacts were made on disordered surfaces, such as the as-prepared surface after the electrochemical reaction [Figs. S4(c) and S4(d)], we observed a widening of the central peak and a lot of sharp dips at the tail, as shown in Figs. S4(a) and S4(b). Those sharp dips have been discussed [37] to be due to the effects of heating and/or critical currents. Although the spectra in Fig. S4 are contaminated by the heating effects, it should be noted that the sharp central part within the two vertical dashed lines in Fig. S4(b) is likely to signify the intrinsic ZBCP, because its width is less than 2 meV and is consistent with twice the gap energy.

## S5. Theoretical calculations of the surface states of $\text{Cu}_x\text{Bi}_2\text{Se}_3$

It is known from the studies of the tunneling spectroscopy of unconventional superconductors [38] that the measured conductance of actual experiments of a point contact between a normal metal and a superconductor corresponds to the local density of states (LDOS) of the superconductor at the surface. Therefore, we theoretically calculate the LDOS of  $\text{Cu}_x\text{Bi}_2\text{Se}_3$  based on a model Hamiltonian for the topological insulator  $\text{Bi}_2\text{Se}_3$  proposed by H. Zhang *et al.* [49]. The Hamiltonian  $\mathcal{H}(\mathbf{k})$  of the present system becomes  $8 \times 8$  matrix, due to the presence of two orbitals, spin indices and electron-hole space [34, 51]. We denote  $\mathcal{H}(\mathbf{k})$  using the  $4 \times 4$  matrices  $\hat{\xi}(\mathbf{k})$  and  $\hat{\Delta}$  as

$$\mathcal{H}(\mathbf{k}) = \begin{pmatrix} \hat{\xi}(\mathbf{k}) & \hat{\Delta} \\ \hat{\Delta}^\dagger & -\hat{\xi}^*(-\mathbf{k}) \end{pmatrix}. \quad (1)$$

	gap type	parity	energy gap structure
$\Delta_1$	$\Delta_{\uparrow\downarrow}^{11} = -\Delta_{\uparrow\uparrow}^{11} = \Delta_{\uparrow\downarrow}^{22} = -\Delta_{\uparrow\uparrow}^{22}$ $\Delta_{\uparrow\downarrow}^{12} = -\Delta_{\uparrow\uparrow}^{12} = -\Delta_{\uparrow\downarrow}^{21} = \Delta_{\uparrow\uparrow}^{21}$	even	full gap
$\Delta_2$	$\Delta_{\uparrow\downarrow}^{12} = -\Delta_{\uparrow\uparrow}^{12} = \Delta_{\uparrow\downarrow}^{21} = -\Delta_{\uparrow\uparrow}^{21}$	odd	full gap
$\Delta_3$	$\Delta_{\uparrow\downarrow}^{12} = \Delta_{\uparrow\uparrow}^{12} = -\Delta_{\uparrow\downarrow}^{21} = -\Delta_{\uparrow\uparrow}^{21}$	odd	point node
$\Delta_4$	$\Delta_{\uparrow\uparrow}^{12} = \Delta_{\uparrow\downarrow}^{12} = -\Delta_{\uparrow\uparrow}^{21} = -\Delta_{\uparrow\downarrow}^{21}$ $\Delta_{\uparrow\uparrow}^{11} = -\Delta_{\uparrow\downarrow}^{11} = -\Delta_{\uparrow\uparrow}^{21} = \Delta_{\uparrow\downarrow}^{21}$	odd	point node

TABLE I: Four types of pair potentials introduced by Hao and Lee [51]. Odd-parity gap functions correspond to unconventional SC states.

The normal-state Hamiltonian  $\hat{\xi}(\mathbf{k})$  is given by

$$\hat{\xi}(\mathbf{k}) = \begin{pmatrix} \varepsilon(\mathbf{k}) + M(\mathbf{k}) & 0 & A_1(\mathbf{k}) & A_2^-(\mathbf{k}) \\ 0 & \varepsilon(\mathbf{k}) + M(\mathbf{k}) & A_2^+(\mathbf{k}) & -A_1(\mathbf{k}) \\ A_1(\mathbf{k}) & A_2^-(\mathbf{k}) & \varepsilon(\mathbf{k}) - M(\mathbf{k}) & 0 \\ A_2^+(\mathbf{k}) & -A_1(\mathbf{k}) & 0 & \varepsilon(\mathbf{k}) - M(\mathbf{k}) \end{pmatrix} \quad (2)$$

with

$$\varepsilon(\mathbf{k}) = \bar{D}_1(2 - 2 \cos(k_z c)) \quad (3)$$

$$+ \frac{4}{3} \bar{D}_2 \left( 3 - 2 \cos\left(\frac{\sqrt{3}}{2} k_x a\right) \cos\left(\frac{1}{2} k_y a\right) - \cos(k_y a) \right) - \mu$$

$$A_1(\mathbf{k}) = \bar{A}_1 \sin(k_z c) \quad (4)$$

$$A_2^\pm(\mathbf{k}) = \frac{2}{3} \bar{A}_2 \quad (5)$$

$$\times \left\{ \sqrt{3} \sin\left(\frac{\sqrt{3}}{2} k_x a\right) \cos\left(\frac{1}{2} k_y a\right) \pm i \left( \cos\left(\frac{\sqrt{3}}{2} k_x a\right) \sin\left(\frac{1}{2} k_y a\right) + \sin(k_y a) \right) \right\}$$

$$M(\mathbf{k}) = M_0 - \bar{B}_1(2 - 2 \cos(k_z c)) \quad (6)$$

$$- \frac{4}{3} \bar{B}_2 \left( 3 - 2 \cos\left(\frac{\sqrt{3}}{2} k_x a\right) \cos\left(\frac{1}{2} k_y a\right) - \cos(k_y a) \right).$$

Note that in the present calculations, we consider the hexagonal lattice with the lattice constants  $a$  and  $c$ , where the 2D triangular lattices stack along the  $c$ -axis direction. We use the same values of parameters  $M_0$ ,  $\bar{A}_2$ ,  $\bar{B}_2$  and  $\bar{D}_2$  as given in Ref. [49], with the transformation  $\bar{A}_2 = A_2/a$ ,  $\bar{B}_2 = B_2/a^2$  and  $\bar{D}_2 = D_2/a^2$ . The values of  $\bar{A}_1$ ,  $\bar{B}_1$ , and  $\bar{D}_1$  are chosen as  $\bar{A}_1 = 0.32$  eV,  $\bar{B}_1 = 0.216$  eV, and  $\bar{D}_1 = 0.024$  eV to fit the energy dispersion for the  $\Gamma - Z$  direction obtained in Ref. [49]. The chemical potential  $\mu$ , which is measured from the Dirac point, was estimated from the experimental data [31] to be  $\mu = 0.5$  eV.

The  $4 \times 4$  pair-potential matrix  $\hat{\Delta}$  is expressed as

$$\hat{\Delta} = \begin{pmatrix} \Delta_{\uparrow\uparrow}^{11} & \Delta_{\uparrow\downarrow}^{11} & \Delta_{\uparrow\uparrow}^{12} & \Delta_{\uparrow\downarrow}^{12} \\ \Delta_{\uparrow\downarrow}^{11} & \Delta_{\uparrow\uparrow}^{11} & \Delta_{\uparrow\downarrow}^{12} & \Delta_{\uparrow\uparrow}^{12} \\ \Delta_{\uparrow\uparrow}^{21} & \Delta_{\uparrow\downarrow}^{21} & \Delta_{\uparrow\uparrow}^{22} & \Delta_{\uparrow\downarrow}^{22} \\ \Delta_{\uparrow\downarrow}^{21} & \Delta_{\uparrow\uparrow}^{21} & \Delta_{\uparrow\downarrow}^{22} & \Delta_{\uparrow\uparrow}^{22} \end{pmatrix}. \quad (7)$$

Upon treating  $\hat{\Delta}$ , we neglect the  $\mathbf{k}$ -dependence for simplicity. Following Hao and Lee [51], we consider the four types of  $\hat{\Delta}$  as shown in Table 1. Note that in Ref. [51] the total number of possible  $\hat{\Delta}$  are six; however, two of them have their counterpart which is the same gap type, so the four types of  $\hat{\Delta}$  summarized in Table 1 are exhaustive. In all the gap types,  $\Delta_{\sigma\sigma'}^{lm} = -\Delta_{\sigma'\sigma}^{ml}$  is satisfied in accordance with the Fermi-Dirac statistics.

To obtain the LDOS, we used the same calculation technique as that employed in Ref. [53]; namely, we calculate the Green's function for the (001) flat surface [which corresponds to the (111) surface in the rhombohedral notation] without disorder, where the momentum parallel to the surface  $\mathbf{k}_\parallel = (k_x, k_y)$  is conserved. The surface Green's function is constructed by introducing an infinite potential barrier at  $z = z_0$ ; with a sufficiently large system size along the

$z$ -direction, one can identify the surface states as the states at  $z = z_1$  which is next to the infinite potential barrier in our lattice calculations. The surface Green's function  $\check{G}_s(\mathbf{k}_\parallel, \omega)$  is obtained from the Fourier-transformed form of the bulk Green's function  $\check{G}_b(z - z'; \mathbf{k}_\parallel, \omega)$  which is written as

$$\check{G}_b(z - z'; \mathbf{k}_\parallel, \omega) = \frac{1}{N_z} \sum_{k_z} \check{G}_b(\mathbf{k}_\parallel, k_z, \omega) e^{ik_z(z-z')}, \quad (8)$$

with

$$\check{G}_b(\mathbf{k}_\parallel, k_z, \omega) = \frac{1}{\omega - \mathcal{H}(\mathbf{k})}, \quad (9)$$

and  $\check{G}_s(\mathbf{k}_\parallel, \omega)$  is given by

$$\begin{aligned} \check{G}_s(\mathbf{k}_\parallel, \omega) &= \check{G}_b(z_1 - z_1; k_y, \omega) \\ &- \check{G}_b(z_1 - z_0; k_y, \omega) \{ \check{G}_b(z_0 - z_0; k_y, \omega) \}^{-1} \check{G}_b(z_0 - z_1; k_y, \omega), \end{aligned} \quad (10)$$

based on the T-matrix method. The resulting momentum-resolved spectral function  $A(\mathbf{k}_\parallel, \omega)$  is given by

$$A(\mathbf{k}_\parallel, \omega) = -\frac{1}{\pi} \sum_{\alpha=1-4} \text{Im} \{ \check{G}_s(\mathbf{k}_\parallel, \omega) \}_{\alpha\alpha}. \quad (11)$$

Finally, we obtain the LDOS  $\rho_s(\omega)$  by integrating  $A(\mathbf{k}_\parallel, \omega)$  over momentum,

$$\rho_s(\omega) = \frac{1}{N_x N_y} \sum_{\mathbf{k}_\parallel} A(\mathbf{k}_\parallel, \omega). \quad (12)$$

In the actual calculations, we took the mesh size of  $N_x = N_y = 516$  and  $N_z = 512$ , and used the maximum gap size,  $\Delta(0)$ , of 0.05 eV for convenience.

Let us discuss the calculated  $A(\mathbf{k}_\parallel, \omega)$  shown in Figs. S5 to S8 for the four gap types. In those figures,  $A(\mathbf{k}_\parallel, \omega)$  is shown by using false colour mapping in arbitrary units along  $\Gamma$ -M and  $\Gamma$ -K directions. For  $\Delta_1$  and  $\Delta_2$ , the excitation spectra have a gap in the bulk [Figs. S5(a) and S6(a)]. At the surface, there is no surface Andreev bound state (ABS) for  $\Delta_1$  [Fig. S5(b)], but the ABS appears as a helical edge mode for  $\Delta_2$  [Fig. S6(b)]. For  $\Delta_3$  and  $\Delta_4$ , the bulk gap closes at certain points on the Fermi surface; namely, those gaps have point nodes [Figs. S7(a) and S8(a)]. Closer examinations of those gap functions find that each has two point nodes at opposing points on the Fermi surface. At the surface for  $\Delta_4$ , one finds an ABS with a partially flat dispersion [Fig. S8(b)]; such a dispersion relation in the ABS can induce a large density of zero-energy states after integrating over  $k_\parallel$  [59]. In contrast, no clear ABS is visible at the surface for  $\Delta_3$  in this calculation [Fig. S7(b)]; however, this does not necessarily mean that the ABS is absent for  $\Delta_3$ . In fact, this is probably because the ABS overlaps with the bulk spectral function (whose contribution is also present at the surface,  $z = z_1$ ), which could make the ABS invisible. (As we discuss in the next section, both the  $\Delta_3$  and  $\Delta_4$  states are topological, so the bulk-edge correspondence dictates that the ABS be present on any surface for  $\Delta_3$  and  $\Delta_4$ .)

In Fig. S9, the resulting LDOS,  $\rho(\omega)$ , is plotted for the two unconventional cases,  $\Delta_2$  [fully-gapped, Fig. S9(a)] and  $\Delta_4$  [point node, Fig. S9(b)]. The  $\Delta_2$  case is similar to the BW-phase in superfluid  $^3\text{He}$  [60] and  $\rho(\omega)$  at the surface has a minimum at zero energy. On the other hand, in the  $\Delta_4$  case with point nodes,  $\rho(\omega)$  has a clear ZBCP, due to the partially-flat dispersion of the ABS.

It should be noted that the results for the  $\Delta_2$  state can change qualitatively when the parameters for the calculations are changed, and for some range of the parameters, a ZBCP was obtained; this is consistent with the very recent proposal by Hsieh and Fu [54]. As an example, we show in Fig. S10 the band dispersions and the LDOS for the bulk and surface states obtained within our model for a different set of parameters. One can see that the surface ABS has a twisted dispersion [Fig. S10(a)] and the surface LDOS shows a three-peak structure with the central peak at zero energy. Therefore, it is probably premature to dismiss the fully-gapped  $\Delta_2$  state as being inconsistent with the experimental data showing a pronounced ZBCP.

## S6. Bulk topological number of the $\Delta_3$ and $\Delta_4$ states with point nodes

Generally, topological phases are characterized by nontrivial topological numbers associated with the global structure of the Hilbert space. Hence, one usually presumes the existence of a non-zero energy gap which separates the topological ground state from its excited states. However, this is not so simple if we consider superconducting states. Indeed, in two dimensions, the existence of a well-defined topological number has been shown even for gapless superconductors [61].

Here, we generalize the arguments in Ref. [61] and show that the superconducting states  $\Delta_3$  and  $\Delta_4$ , both of which have point nodes in the gap, support a well-defined topological number. Our finding indicates that the gapless surface states of these superconductors are topologically protected. In other words, they are topological superconductors.

Before examining the nodal superconductors, we briefly review the topological number for *fully-gapped* 3D time-reversal-invariant superconductors. The topological number is defined on the basis of the symmetry of the Bogoliubov-de Gennes (BdG) Hamiltonian. A fundamental character of the BdG Hamiltonian is the particle-hole symmetry

$$\mathcal{C}\mathcal{H}(\mathbf{k})\mathcal{C}^\dagger = -\mathcal{H}^*(-\mathbf{k}), \quad (13)$$

where  $\mathcal{C}$  is the charge conjugation matrix. In addition, in time-reversal-invariant superconductors, the BdG Hamiltonian has the time-reversal symmetry

$$\Theta\mathcal{H}(\mathbf{k})\Theta^\dagger = \mathcal{H}^*(\mathbf{k}), \quad (14)$$

with  $\Theta\Theta^T = -1$ . Combining these symmetries, one obtains the so-called chiral symmetry,

$$\{\mathcal{H}(\mathbf{k}), \Gamma\} = 0, \quad \Gamma = \Theta\mathcal{C}. \quad (15)$$

This chiral symmetry plays the central role in the definition of the topological number. Let us consider the BdG equation,

$$\mathcal{H}(\mathbf{k})|u_n(\mathbf{k})\rangle = E_n(\mathbf{k})|u_n(\mathbf{k})\rangle. \quad (16)$$

When the chiral symmetry is present, one obtains

$$\mathcal{H}(\mathbf{k})\Gamma|u_n(\mathbf{k})\rangle = -E_n(\mathbf{k})\Gamma|u_n(\mathbf{k})\rangle, \quad (17)$$

which means that if  $|u_n(\mathbf{k})\rangle$  is a quasiparticle state with positive energy  $E_n > 0$ , then  $\Gamma|u_n(\mathbf{k})\rangle$  is a quasiparticle state with negative energy. We use a positive  $n$  (negative  $n$ ) for  $|u_n(\mathbf{k})\rangle$  to represent a positive (negative) energy quasiparticle state, and set

$$|u_{-n}(\mathbf{k})\rangle = \Gamma|u_n(\mathbf{k})\rangle. \quad (18)$$

The topological number is defined by using the following  $Q$  matrix,

$$Q(\mathbf{k}) = \sum_{n>0} |u_n(\mathbf{k})\rangle\langle u_n(\mathbf{k})| - \sum_{n<0} |u_n(\mathbf{k})\rangle\langle u_n(\mathbf{k})|. \quad (19)$$

From Eq. (18), we have  $\{Q(\mathbf{k}), \Gamma\} = 0$ . Hence, if we take the basis in which  $\Gamma$  is diagonalized as

$$\Gamma = \begin{pmatrix} 1 & 0 \\ 0 & -1 \end{pmatrix}, \quad (20)$$

then  $Q(\mathbf{k})$  becomes off-diagonal

$$Q(\mathbf{k}) = \begin{pmatrix} 0 & q(\mathbf{k}) \\ q^\dagger(\mathbf{k}) & 0 \end{pmatrix}, \quad (21)$$

where  $q(\mathbf{k})$  is a unitary matrix because  $Q(\mathbf{k})$  satisfies  $Q^2(\mathbf{k}) = 1$ . The topological number is defined as the winding number of the unitary matrix  $q(\mathbf{k})$  [26],

$$w_{3d} = \frac{1}{24\pi^2} \int d^3k \epsilon^{ijk} \text{tr}[q\partial_i q^\dagger q\partial_j q^\dagger q\partial_k q^\dagger]. \quad (22)$$

Here, note that the above definition of the topological number is possible only when the system is fully gapped. Otherwise, the positive energy states can not be separated from the negative ones, and the  $Q(\mathbf{k})$  matrix is not well defined.

Now let us try to define the same topological number for nodal superconductors such as  $\Delta_3$  and  $\Delta_4$ . The simplest way to do this is to introduce a small perturbation to eliminate all nodes in the spectrum. For time-reversal-invariant superconductors, point nodes are not topologically protected, so we can always open a gap by a small deformation of the gap functions.<sup>1</sup> After removing the nodal points, the winding number  $w_{3d}$  can be evaluated in the manner shown above. This simple procedure, however, does not work after all. The problem is that the value of the winding number depends on the perturbation we choose. As a result, one cannot have a unique definition of the winding number for gapless systems.

On the other hand, we find that this procedure does define the *mod-2 winding number* (*i.e.*, parity of the winding number) uniquely. The point is that we always have point nodes in pairs: From the time-reversal invariance (or particle-hole symmetry), if we have a point node  $K$  at  $\mathbf{k} = \mathbf{k}_0$ , then we have another node  $K'$  at  $\mathbf{k} = -\mathbf{k}_0$ . Thus, even if the point node  $K$  may cause the ambiguity of integer  $N$  in the winding number, the total ambiguity is always  $2N$ . Therefore, the mod-2 winding number is not affected by the ambiguity of this procedure.

Actually, the above statement can be shown rigorously. For this purpose, we introduce the ‘‘gauge field’’  $A_i(\mathbf{k})$ ,

$$A_i(\mathbf{k})_{mn} = i\langle u_m(\mathbf{k}) | \partial_i u_n(\mathbf{k}) \rangle, \quad (23)$$

and consider the ‘‘Chern-Simons term’’,

$$S_{CS} = \frac{1}{16\pi^2} \int d^3k \epsilon^{ijk} \text{tr}[(F_{ij} + \frac{2}{3}iA_iA_j)A_k], \quad (24)$$

with  $F_{ij} = \partial_i A_j - \partial_j A_i - i[A_i, A_j]$ . Here the matrix multiplication and the trace are done for negative  $n$  (*i.e.*, negative energy states). To see how the Chern-Simons term is related to the winding number, consider the following eigenstate of  $Q(\mathbf{k})$  with the eigenvalue  $-1$ :

$$|\psi_n(\mathbf{k})\rangle = \frac{1}{\sqrt{2}} \begin{pmatrix} \phi_n \\ -q^\dagger(\mathbf{k})\phi_n \end{pmatrix}, \quad (25)$$

where  $\phi_n$  is a  $\mathbf{k}$ -independent orthogonal basis vector, *i.e.*,  $\phi_n^\dagger \phi_m = \delta_{mn}$ . Because a negative energy state  $|u_n(\mathbf{k})\rangle$  ( $n < 0$ ) is also an eigenstate of  $Q(\mathbf{k})$  with the eigenvalue  $-1$ , we can expand it with  $|\psi_n(\mathbf{k})\rangle$  as

$$|u_n(\mathbf{k})\rangle = \sum_m |\psi_m(\mathbf{k})\rangle U_{mn}(\mathbf{k}), \quad (26)$$

with a unitary matrix  $U(\mathbf{k})$ . From the definition of the gauge field, we have

$$A_i(\mathbf{k}) = iU^\dagger \partial_i U + U^\dagger a_i(\mathbf{k})U, \quad a_i(\mathbf{k}) = \frac{i}{2}q \partial_i q^\dagger. \quad (27)$$

Substituting Eq. (27) into Eq. (24) yields

$$\begin{aligned} S_{CS} &= \frac{1}{16\pi^2} \int d^3k \epsilon^{ijk} \text{tr}[(F_{ij} + \frac{2}{3}iA_iA_j)A_k] \\ &= \frac{1}{16\pi^2} \int d^3k \epsilon^{ijk} \text{tr}[(f_{ij} + \frac{2}{3}ia_ia_j)a_k] + \frac{1}{24\pi^2} \int d^3k \text{tr}[U^\dagger \partial_i U U^\dagger \partial_j U U^\dagger \partial_k U] \\ &= \frac{1}{48\pi^2} \int d^3k \epsilon^{ijk} \text{tr}[q \partial_i q^\dagger q \partial_j q^\dagger q \partial_k q^\dagger] + \frac{1}{24\pi^2} \int d^3k \text{tr}[U^\dagger \partial_i U U^\dagger \partial_j U U^\dagger \partial_k U]. \end{aligned} \quad (28)$$

Here we have used the fact that in a time-reversal-invariant system the global basis of wave functions exists on a torus  $T^3$  [62], and hence the total derivative term does not contribute to the integration. Remembering that the second term in the third line of the right hand side of Eq. (28) is the winding number of  $U$ , we obtain

$$S_{CS} = \frac{1}{2}w_{3d} + N, \quad (29)$$

---

<sup>1</sup> Note that this is not possible when the time-reversal-symmetry is broken. For instance, the point nodes in the  $^3\text{He}$  A-phase cannot be removed by small perturbations, since they have their own topological number. The time-reversal invariance is crucial in the argument in this section.

where  $N$  is an integer denoting the winding number of  $U$ . The above relation (29) means that the mod-2 winding number is simply given by the parity of twice the Chern Simons term,

$$(-1)^{w_{3d}} = (-1)^{2S_{\text{SC}}}. \quad (30)$$

Now we employ a useful relation derived for topological insulators by Wang, Qi and Zhang, who showed [62] that the parity of twice the Chern-Simons term coincides with the  $\mathbf{Z}_2$  invariant given by Fu, Kane and Mele [?] and by Moore and Balents [?]. The  $\mathbf{Z}_2$  invariant is expressed by the Pfaffians of the following unitary matrix between the occupied states,

$$w_{mn}(\mathbf{k}) = \langle u_m(-\mathbf{k}) | \Theta | u_n^*(\mathbf{k}) \rangle. \quad (31)$$

Because of the identity  $\Theta\Theta^T = -1$ ,  $w_{nm}(\mathbf{k})$  becomes antisymmetric at the time-reversal-invariant momentum (TRIM)  $\Gamma_i$ , which makes it possible to define the Pfaffians at these points. The  $\mathbf{Z}_2$  invariant  $\nu_0$  is given by

$$(-1)^{\nu_0} = \prod_{i=1}^8 \delta_i, \quad \delta_i = \frac{\sqrt{\det[w(\Gamma_i)]}}{\text{Pf}[w(\Gamma_i)]}, \quad (32)$$

where the product is taken for all the TRIMs in the Brillouin zone. The relation given by Wang, Qi and Zhang [62] is

$$(-1)^{2S_{\text{SC}}} = (-1)^{\nu_0}. \quad (33)$$

Combining Eqs. (30) and (33), one obtains

$$(-1)^{w_{3d}} = \prod_i^8 \frac{\sqrt{\det[w(\Gamma_i)]}}{\text{Pf}[w(\Gamma_i)]}. \quad (34)$$

This expression, Eq. (34), indicates that  $(-1)^{w_{3d}}$  depends only on the wave function at the special points  $\Gamma_i$  in the Brillouin zone, *i.e.*, the TRIMs. On the other hand, a perturbation to remove a node may only affect the local structure of the wave function near the gap node. Therefore, Eq. (34) suggests that  $(-1)^{w_{3d}}$  could be independent of the perturbation since the node is not located at  $\Gamma_i$  in general.

To make the argument rigorous, we explicitly consider an odd-parity superconductor. For odd-parity superconducting states such as  $\Delta_3$  and  $\Delta_4$ , we have the following additional symmetry in the BdG Hamiltonian

$$\Pi \mathcal{H}(\mathbf{k}) \Pi^\dagger = \mathcal{H}(-\mathbf{k}), \quad (35)$$

where  $\Pi$  is given by the parity operator  $P$  as

$$\Pi = \begin{pmatrix} P & 0 \\ 0 & -P^* \end{pmatrix}. \quad (36)$$

Here we have used the fact that odd-parity superconductors satisfy  $P\Delta(\mathbf{k})P^* = -\Delta(-\mathbf{k})$ . In our BdG Hamiltonian [51],  $P = s_0 \otimes \sigma_3$ . At the TRIM  $\Gamma_i$ , Eq. (35) reduces to  $[\mathcal{H}(\Gamma_i), \Pi] = 0$ , which means that the quasiparticle state  $|u_n(\Gamma_i)\rangle$  is simultaneously an eigenstate of  $\Pi$ , *i.e.*,  $\Pi|u_n(\Gamma_i)\rangle = \pi_n(\Gamma_i)|u_n(\Gamma_i)\rangle$ . Now let us consider the following matrix

$$P_{mn} = \langle u_m(\mathbf{k}) | \Pi^\dagger \Theta | u_n^*(\mathbf{k}) \rangle, \quad (37)$$

which is connected to  $w_{mn}$  at the TRIM  $\Gamma_i$  via

$$P_{mn}(\Gamma_i) = \pi_m(\Gamma_i)w_{mn}(\Gamma_i). \quad (38)$$

Taking the Pfaffians on both sides yields

$$\text{Pf}[P(\Gamma_i)] = \text{Pf}[w(\Gamma_i)] \prod_m \pi_{2m}(\Gamma_i), \quad (39)$$

which leads to

$$\prod_i \frac{\sqrt{\det[w(\Gamma_i)]}}{\text{Pf}[w(\Gamma_i)]} = \prod_i \frac{\text{Pf}[P(\Gamma_i)]}{\sqrt{\det[P(\Gamma_i)]}} \prod_m \pi_{2m}(\Gamma_i). \quad (40)$$

We find here that the term  $\text{Pf}[P(\Gamma_i)]/\sqrt{\det[P(\Gamma_i)]}$  gives rise to only a trivial factor. Indeed, by direct calculations, one obtains

$$\text{tr}A_i(\mathbf{k}) = -i\partial_i \ln \text{Pf}[P(\mathbf{k})]. \quad (41)$$

Thus, by taking the  $\text{tr}A_i(\mathbf{k}) = 0$  gauge [which is consistent with the relation  $\text{tr}F_{ij}(\mathbf{k}) = 0$  obtained by the symmetries (14) and (35)], one can see that  $\text{Pf}[P(\mathbf{k})]$  is independent of  $\mathbf{k}$ . Consequently,  $\text{Pf}[P(\Gamma_i)]/\sqrt{\det[P(\Gamma_i)]}$  is factorized in Eq. (40), which results in a trivial factor 1. Therefore, one obtains the final expression

$$(-1)^{w_{3d}} = \prod_{i,m} \pi_{2m}(\Gamma_i). \quad (42)$$

Now we can confirm explicitly that the mod-2 winding number is independent of any weak perturbation  $\delta$  we choose: The parity of the wave function at the TRIM  $\Gamma_i$  is determined locally by the BdG equation at  $\Gamma_i$ , and hence it should not be affected by any small perturbation away from the  $\Gamma_i$  point. This means that we have a unique value of the mod-2 winding number in the limit of  $\delta \rightarrow 0$ , *i.e.*, the mod-2 winding number is well-defined even in the presence of point nodes, although the winding number  $w_{3d}$  itself is not. Therefore, a time-reversal-invariant superconductor with a pair (or pairs) of point nodes can be robustly topological if the parity of the gap function is odd.

In a weak paring state, we can evaluate  $(-1)^{w_{3d}}$  rather easily. In this case,  $\prod_{i,m} \pi_{2m}(\Gamma_i)$  can be expressed in terms of the energy dispersion of the system in the normal state [27, 63], which leads to

$$(-1)^{w_{3d}} = \prod_{i,m} \text{sgn}[\mathcal{E}_{2m}(\Gamma_i)]. \quad (43)$$

Here  $\mathcal{E}_{2m}(\mathbf{k})$  is the normal-state energy dispersion obtained as an eigenvalue of  $\hat{\xi}(\mathbf{k})$  [defined in Eq. (2)], and the Kramers degeneracy is taken into account as  $\mathcal{E}_{2m}(\Gamma_i) = \mathcal{E}_{2m+1}(\Gamma_i)$ . In our model Hamiltonian, we obtain  $\prod_{i,m} \text{sgn}[\mathcal{E}_{2m}(\Gamma_i)] = -1$ . Thus, all the odd-parity superconducting states  $\Delta_2$ ,  $\Delta_3$  and  $\Delta_4$  given in Table 1 have a non-trivial topological number  $(-1)^{w_{3d}} = -1$ , indicating that all of them are topological superconductors irrespective of the presence of the point nodes.

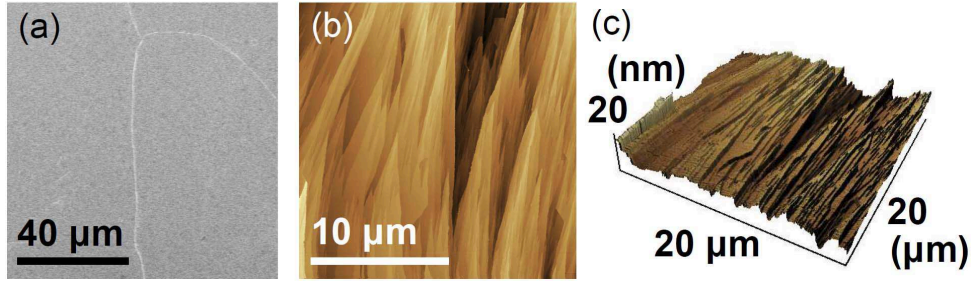


FIG. S1: Cleaved surface of  $\text{Cu}_x\text{Bi}_2\text{Se}_3$ . Scanning-electron microscope finds that the cleaved surface of  $\text{Cu}_x\text{Bi}_2\text{Se}_3$  is essentially flat (a). However, atomic-force microscope finds a lot of nanometer-scale terraces in the “flat” region (b). 3D presentation of the data in panel b is shown in panel (c), where the vertical variation is very much exaggerated.

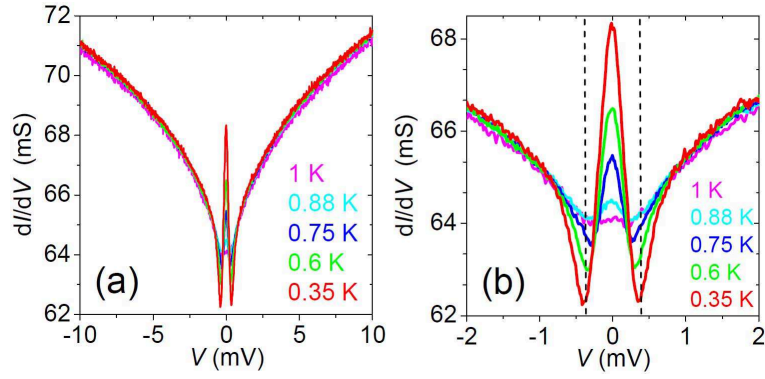


FIG. S2: Additional ZBCP data of  $\text{Cu}_x\text{Bi}_2\text{Se}_3$ . (a, b) Spectra showing the ZBCP in 0 T measured on a sample different from that reported in the main text. (a) is for a wide energy window, and (b) magnifies the low energy range. The dashed lines in b indicate the energy position of the dips.

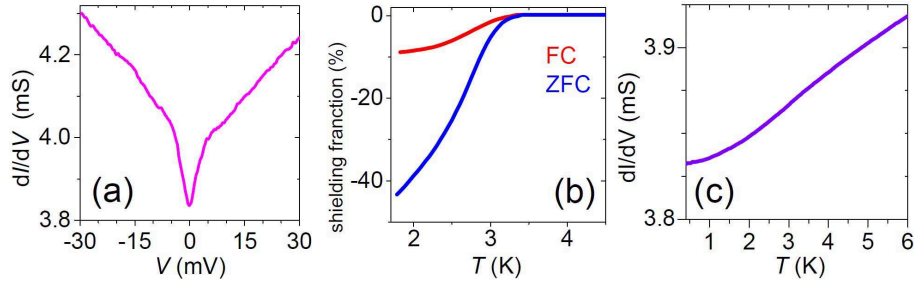


FIG. S3: An example of the point-contact spectrum at 0.35 K showing no feature associated with superconductivity (a), measured on a sample with the bulk onset  $T_c$  of 3.2 K (b). The temperature dependence of the conductance of this point contact at zero bias showed no sign of superconductivity (c), suggesting that the portion of the sample beneath this point contact was non-superconducting.

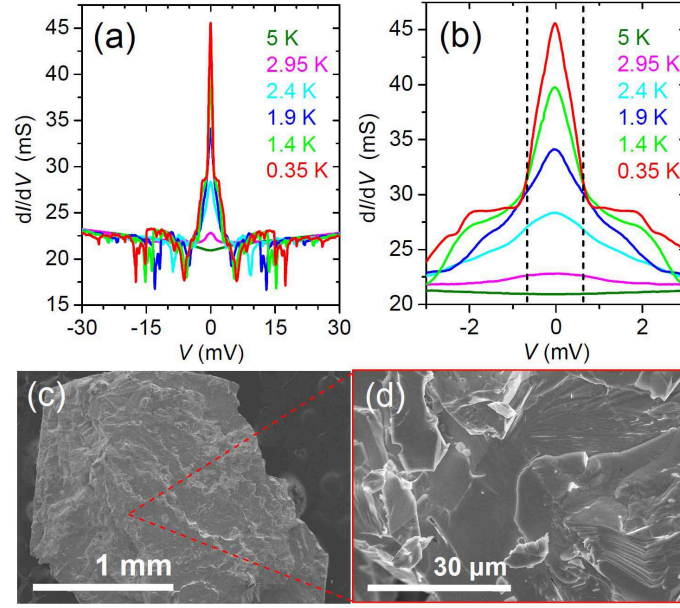


FIG. S4: Spectra of a point contact made on the as-intercalated surface of  $\text{Cu}_x\text{Bi}_2\text{Se}_3$ . (a, b)  $dI/dV$  vs bias voltage for 0.35 - 5 K measured in 0 T for a wide energy window is shown in (a), and (b) magnifies the data near zero energy; the vertical dashed lines indicate the sharp central part of the spectra in (b). The as-intercalated surfaces are rough even under the optical microscope; (c) is a scanning-electron-microscope picture of a typical as-intercalated surface, and (d) is a magnified picture of a spot in (c).

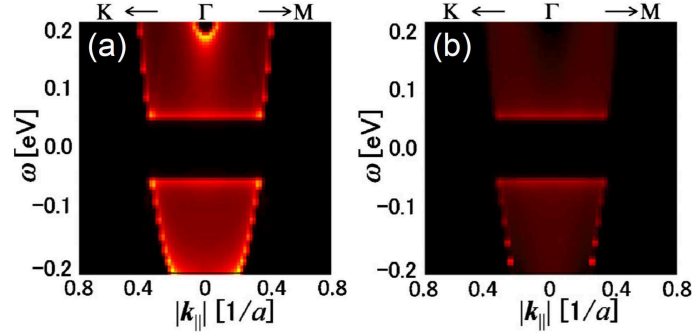


FIG. S5: Spectral functions  $A(\mathbf{k}_{\parallel}, \omega)$  for the pair potential  $\Delta_1$  ( $\Delta_{\uparrow\downarrow}^{11} = -\Delta_{\downarrow\uparrow}^{11} = \Delta_{\uparrow\downarrow}^{22} = -\Delta_{\downarrow\uparrow}^{22}$ ). (a) bulk, (b) surface.

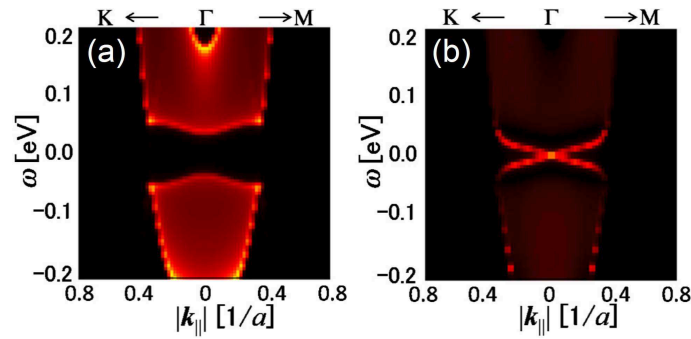


FIG. S6: Spectral functions  $A(\mathbf{k}_{\parallel}, \omega)$  for the pair potential  $\Delta_2$ . (a) bulk, (b) surface.

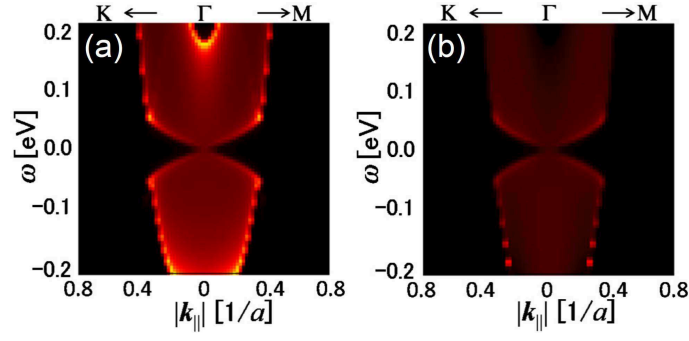


FIG. S7: Spectral functions  $A(\mathbf{k}_{\parallel}, \omega)$  for the pair potential  $\Delta_3$ . (a) bulk, (b) surface.

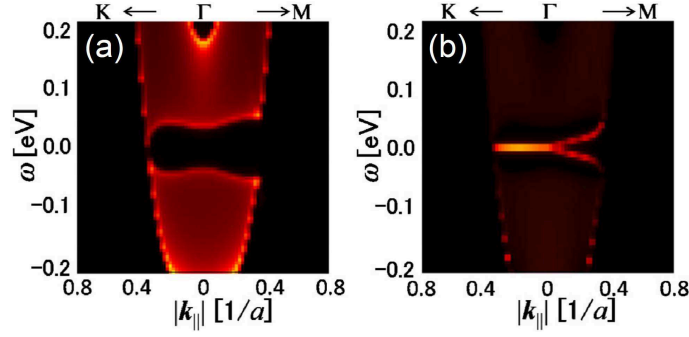


FIG. S8: Spectral functions  $A(\mathbf{k}_{\parallel}, \omega)$  for the pair potential  $\Delta_4$  ( $\Delta_{\uparrow\uparrow}^{12} = \Delta_{\downarrow\downarrow}^{12} = -\Delta_{\uparrow\uparrow}^{21} = -\Delta_{\downarrow\downarrow}^{21}$ ). (a) bulk, (b) surface.

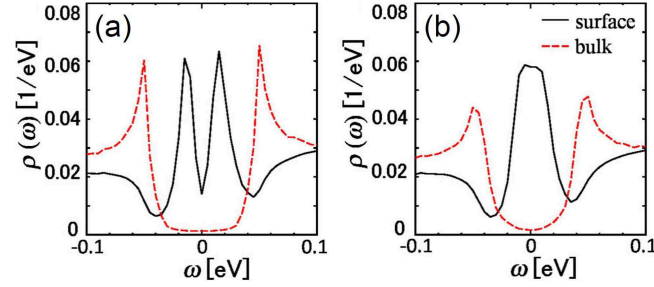


FIG. S9: Calculated local density of states. (a, b) LDOS at the bulk (dashed line) and the surface (solid line) for the pair potentials  $\Delta_2$  [panel (a)] and  $\Delta_4$  [panel (b)].

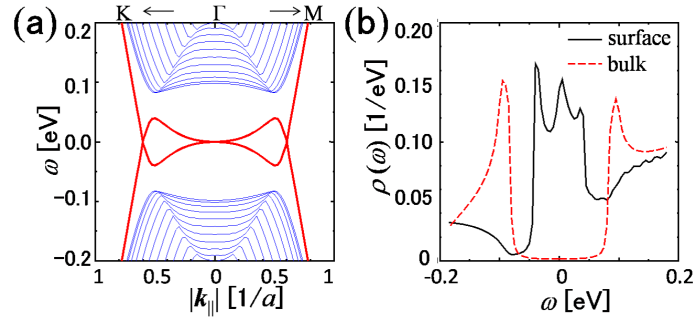


FIG. S10: Calculation results for the pair potential  $\Delta_2$  with  $\bar{D}_1 = \bar{D}_2 = 0$ ,  $\bar{A}_1 = 1.0$ ,  $\bar{A}_2 = 1.5$ ,  $M_0 = -0.7$ ,  $\bar{B}_1 = 0.5$ ,  $\bar{B}_2 = 0.75$ ,  $\mu = 0.9$ , and  $\Delta(0) = 0.1$  (all in eV). (a) Band dispersions for the bulk (blue) and the surface (red). (b) LDOS at the bulk (dashed line) and the surface (solid line).